



HAL
open science

An experimental evidence of the failure of Cauchy elasticity for the overall modeling of a non-centro-symmetric lattice under static loading

M. Poncelet, A Somera, C. Morel, C Jailin, Nicolas Auffray

► To cite this version:

M. Poncelet, A Somera, C. Morel, C Jailin, Nicolas Auffray. An experimental evidence of the failure of Cauchy elasticity for the overall modeling of a non-centro-symmetric lattice under static loading. *International Journal of Solids and Structures*, 2018, 147, pp.223-237. 10.1016/j.ijsolstr.2018.05.028 . hal-01704787v2

HAL Id: hal-01704787

<https://hal.science/hal-01704787v2>

Submitted on 31 May 2018

HAL is a multi-disciplinary open access archive for the deposit and dissemination of scientific research documents, whether they are published or not. The documents may come from teaching and research institutions in France or abroad, or from public or private research centers.

L'archive ouverte pluridisciplinaire **HAL**, est destinée au dépôt et à la diffusion de documents scientifiques de niveau recherche, publiés ou non, émanant des établissements d'enseignement et de recherche français ou étrangers, des laboratoires publics ou privés.

An experimental evidence of the failure of Cauchy elasticity for the overall modeling of a non-centro-symmetric lattice under static loading

M. Poncelet^a, A. Somera^a, C. Morel^a, C. Jailin^a, N. Auffray^{b,*}

^a*LMT (ENS Paris-Saclay/CNRS/Université Paris Saclay), 61 avenue du Président Wilson, F-94235 Cachan, France*

^b*Université Paris-Est, Laboratoire Modélisation et Simulation Multi Echelle, MSME UMR 8208 CNRS, 5 bd Descartes, 77454 Marne-la-Vallée, France*

Abstract

Materials with coarse inner architecture being easily made with modern additive or folding processes, the question of their overall behavior rises. Do they behave like classical elastic continua, or do they exhibit additional higher-order effects ? Further, if present are those effects stable with respect to imperfections (geometry, constitutive material, ...) ? In this view, the current work is an experimental investigation for the need, in static, of a higher-order overall description. It comes from noticing that such behaviors are up to now nearly exclusively studied from a theoretical and numerical point of view. In the present study a non-centro symmetric sample has been manufactured, based on an industrial honeycomb geometry used for aeronautic/aerospace composite materials. The geometrical anisotropy of the elementary cell and the scale separation ratio have been chosen in order to detect non-classical couplings. Samples are obtained by Fused Deposition Modeling (FDM), one of the most widespread 3D printing techniques. Simple experiments based on load controlled tests with full-field kinematic measurement have been performed. A distributed load control reveals that the overall behavior of the architected material cannot be described within the realm of Cauchy elasticity.

Keywords: strain-gradient elasticity, Anisotropy, Boundary Conditions, Full-field measurement, Architected materials, Non-centrosymmetric lattices, Generalized continua.

1. Introduction

Several scales are often use to model a material:

*Corresponding author

- The macroscale, which is fundamentally defined by the characteristic scale of the considered loading. Its characteristic length is thereafter written M .
- The microscale, which is an arbitrary cut-off below which matter will be supposed continuous (and modelled as such). Its characteristic length is thereafter written μ . Below this scale, from a physical point of view, the matter is still organized, but the precise details of this organization are ‘forgotten’ in the modelling.
- The mesoscale(s) which lie(s) between the micro and the macro ones. One may found several mesoscales. In the case of a single mesoscale, its characteristic length is thereafter written m .

Based on these definitions, a material is said to be architected if:

1. it presents, between its microstructure and its macrostructure, one or more other scales of organization of matter;
2. the intermediate scales of organization are comparable with those of the macrostructure, but separate with the one of the microstructure.

As a consequence the overall physical properties of architected materials are defined by the choice of constitutive materials, and of an inner structure. From a design point of view, it is often valuable to substitute the original architected material by an homogeneous equivalent one. The interests are the emergence of relevant design parameters and gains in time computations, resulting in an easier exploration of their design space.

If the different scales are well-separated *i.e.* $\mu \ll M$ (Fig. 1(a)), the determination of the overall elastic continuum is direct within the classical theory of homogenization¹ [7]. In this situation, the overall homogeneous medium is a classical elastic continuum (*a.k.a* Cauchy continuum), meaning that most of the structural effects are lost going from the scale of the architecture to the one of the sample.

¹Even if this point will not be discussed further in this paper, the situation is a bit more complex. Classical theorems in the mathematical theory of homogenization holds for a vanishing small scale separation ratio ($\epsilon \rightarrow 0$) and provided the elasticity tensor field is strictly positive definite almost everywhere (and its inverse) [3]. Porous materials, having voids as phases, do not fit into these hypotheses. Further it can be proved that the homogenization limit can be, in such a case, non-classical, even under the scale separation hypothesis [28, 9].

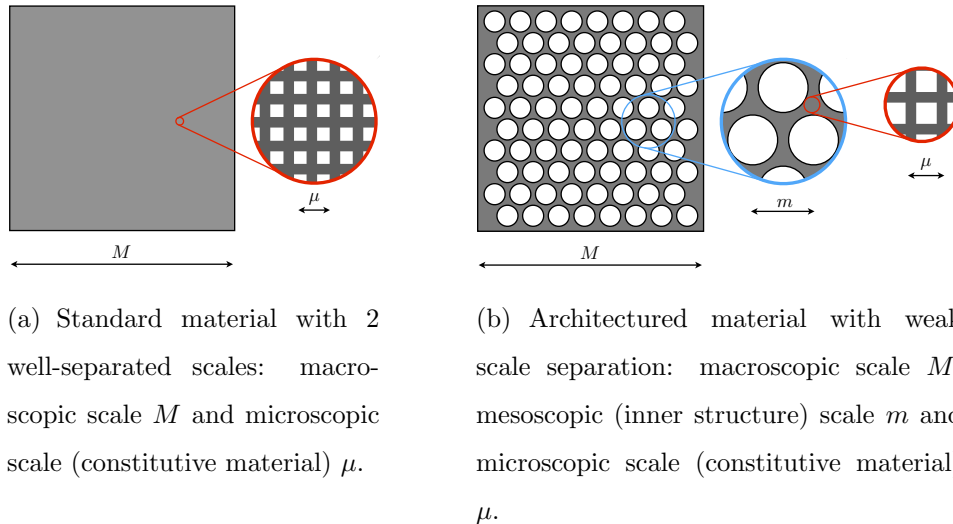


Figure 1: The different scales of materials. The red magnification lens shows the microscopic scale which is modeled with a constitutive law, while the blue shows the mesoscale which is described by its geometry.

On the contrary, in case of weak scale separation *i.e.* $\mu \ll m \lesssim M$ (Fig. 1(b)), structural effects cannot be neglected at the macro level and the classical Cauchy continuum has to be enriched in some way for the overall elastic behaviour to be well-described. In literature there are numerous references dealing with this issue from a theoretical point of view [11, 19, 23, 16, 1]. But, what about the practical needs for such enrichment ?

In elastodynamics, the insufficiency of Cauchy elasticity are rather clear [23, 27, 32, 33]. Considering wave propagation in lattices, the influence of the architecture is revealed by the band structure of the dispersion diagram. As well known, the classical Cauchy elasticity can not reproduce these effects. This motivates, in the 70', the development of generalized continuum theories [23, 25]. In a recent contribution [32], it has been shown that Cauchy elasticity is unable to reproduce the hexagonal wave propagation that has been observed both numerically and experimentally in honeycomb structures. In the same reference, it is shown that an extension of classical elasticity, called strain-gradient elasticity, is able to model the observed phenomenon. In [33], the validity range of this enrichment is studied. It results that the use of a strain-gradient continuum as an overall medium improves the continuous description for scale separation ratios ($\epsilon = \frac{m}{M}$) between 1/6 and 1/20. For ratios less than 1/20 the standard Cauchy description is sufficient, while for ratios greater than 1/6 strain-gradient elasticity is no more satisfactory.

If the need for generalized continua in elastodynamics is clear, its relevance for static situations is still open. So the question is, can we find situations for which classical

elasticity fails to correctly describe the observed phenomenon ? Hence, the aim of the present contribution is double:

1. identify a non-fictitious situation for which an overall Cauchy description would fail;
2. verify, for this situation, if the predicted discrepancy can be experimentally evidenced.

The non-fictitious feature stands for a situation that may be found in everyday life or industrial domain as opposed to a purely academic case. For example, the interesting pantograph structure [2, 1, 31, 29] has already been studied in a static way, but is still considered as an exotic illustration of the theory. The possibility of an experimental observation is questioned because of the multiple sources of dispersions: geometry, material parameters, boundary conditions and mechanical loading. So the goal is to check whether the higher-order effects evidenced on theoretical/numerical grounds do emerge in experimental testing or if they are hidden by the numerous dispersions.

Such a situation might be the following. It is well known that classical elasticity is non sensitive to the lack of centro-symmetry of the microstructure. It can be shown that extending classical elasticity by considering higher-gradients of the displacement field into the energetic formulation will make the behavior sensitive to centro-symmetry. The establishment of strain-gradient elasticity from asymptotic expansion [8, 38] shows that the fifth-order tensor responsible for this coupling is of order ϵ in the expansion, and hence dominant when compared to the second-order elasticity tensor which is ϵ^2 in the expansion. Hence, as an Ockham razor, a sample of a non centro-symmetric architected material with weak scale separation will be tested in homogeneous tension.

If the resulting strain field is homogeneous the overall continuum is of Cauchy type, if not, a generalized continuum should be considered. This test will first be considered numerically and then checked experimentally. Concerning the experimental procedure two samples of architected materials having different symmetry classes (centro and non-centro-symmetric) will be made by Rapid Prototyping Technology (RPT). The use of a Fused Deposition Modeling (FDM) technique will lead to a rather fine (external) shape accuracy but poor (inner) constitutive matter quality because of its highly non uniform porosity. This realistic but far-from-perfect state is considered interesting to test the high-order behavior sensitivity to defects. Last, as we aim at "observing" the constitutive law, samples will be loaded in force in order to be observed, via Digital Image Correlation

(DIC), the associated kinematic fields.

Organization of the paper

The paper is organized as follows. In a first section, §.2, the conceptual setting of an experiment to probe the relevance of overall Cauchy elastic modeling is introduced. Some notions concerning generalized continuum are presented before detailing the anisotropic formulation of strain-gradient elasticity. For our need the constitutive law is introduced in its compliance form. The anisotropic systems producing coupling between strain-gradient and stress are identified, and the symmetry class for our architected material decided. At the end, two patterns are chosen. One is centro-symmetric, with an expected classical response under uniaxial tension, the other is non-centro-symmetric, with an expected non-standard response. A weak-scale separation ratio ($\epsilon = \frac{m}{M} = \frac{1}{8}$) is considered for producing both the numerical and the experimental sample. This ratio lies between the bounds identified in [33] and is chosen so as to magnify the higher-order kinematics. For both materials, numerical uniaxial tension tests are performed in order to design the real experiment.

It is shown, numerically, that Cauchy elasticity cannot serve as an overall elastic continuum to describe the considered experiment. To validate this result, in §.3, an experiment is set up. Two 3D printed architected materials are tested with a load control in the elastic regime. An integrated DIC setup allows to capture the displacement fields and highlights the failure of the homogenized Cauchy model in the second experiment.

Before getting into the core our object, let us introduce some notations:

Notations

In this work tensors of order ranking from 0 to 6 are denoted, respectively, by \mathbf{a} , $\underline{\mathbf{a}}$, $\tilde{\mathbf{a}}$, $\underline{\underline{\mathbf{a}}}$, $\underline{\underline{\underline{\mathbf{a}}}}$ and $\underline{\underline{\underline{\underline{\mathbf{a}}}}}$. The simple, double, third and fourth contractions are written \cdot , $:$, $\cdot\cdot$ and $::$ respectively. In index form with respect to an orthonormal Cartesian basis, these notations correspond to

$$\underline{\mathbf{a}} \cdot \underline{\mathbf{b}} = a_i b_i, \quad \tilde{\mathbf{a}} : \tilde{\mathbf{b}} = a_{ij} b_{ij}, \quad \underline{\underline{\mathbf{a}}} \cdot\cdot \underline{\underline{\mathbf{b}}} = a_{ijk} b_{ijk}, \quad \underline{\underline{\underline{\mathbf{a}}}} :: \underline{\underline{\underline{\mathbf{b}}}} = a_{ijkl} b_{ijkl}$$

where repeated indices are summed up. More generally p -order contraction between two tensors \mathbf{A} and \mathbf{B} of respective orders n and m ($p \leq \min(n, m)$)

$$(\mathbf{A} \odot^p \mathbf{B})_{i_1 \dots i_{n-p} j_{p+1} \dots j_m} := A_{i_1 \dots i_{n-p} q_1 \dots q_p} B_{q_1 \dots q_p j_{p+1} \dots j_m}$$

where \odot^p is the generalized dot product which reduces to \cdot , $:$, $\cdot:$ and $::$, for $p = \{1, 2, 3, 4\}$. For forthcoming use, the following definition for the transposition of a fifth-order tensor will be retained:

$$(M^T)_{ijklm} := M_{klmij}$$

Spatial derivative will classically be denoted, in index form, by a comma

$$\text{Grad } \underline{\mathbf{a}} = (\underline{\mathbf{a}} \otimes \underline{\nabla})_{ij} = a_{i,j} \quad ; \quad \text{Div } \underline{\mathbf{a}} = (\underline{\nabla} \cdot \underline{\mathbf{a}}) = a_{i,i}$$

The following groups will be considered:

- $O(2)$: the orthogonal group, that is the group of all isometries of \mathbb{R}^2 i.e. $Q \in O(2)$ if $\det(Q) = \pm 1$ and $Q^{-1} = Q^T$, where the superscript T denotes the transposition. As a matrix group $O(2)$, can be generated by:

$$R(\theta) = \begin{pmatrix} \cos \theta & -\sin \theta \\ \sin \theta & \cos \theta \end{pmatrix}, \quad 0 \leq \theta < 2\pi, \quad \text{and} \quad M_y = \begin{pmatrix} -1 & 0 \\ 0 & 1 \end{pmatrix}$$

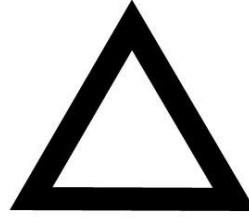
in which $R(\theta)$ is a rotation of θ angle and M_y is the reflection across the y axis;

- Id, the identity group;
- $SO(2)$: the special orthogonal group, i.e. the subgroup of $O(2)$ of elements satisfying $\det(Q) = 1$. This is the group of 2D rotations generated by $R(\theta)$;
- Z_k , the cyclic group with k elements generated by $R(2\pi/k)$, a rotation angle $2\pi/k$ (Fig. 2(a));
- Z_2^π , is the cyclic group generated by the mirror operation M_y . The exponent π is used to differentiate² this group from the one generated by $R(\pi)$;
- D_k , the dihedral group with $2k$ elements generated by $R(2\pi/k)$ and M_y (Fig. 2(b)). Z_k is thus a subgroup of D_k .

²It has to be noted that Z_2^π and Z_2 are isomorphic as group but not conjugate.



(a) A Z_3 -invariant figure



(b) A D_3 -invariant figure

Figure 2: Difference between Z_k - and D_k -invariant patterns

2. Cauchy probing

To probe Cauchy elasticity, it is needed to:

1. *embed* Cauchy elasticity into a generalized elastic continuum;
2. define experiments having identical solutions for Cauchy elasticity that differ for the generalized model.

2.1. Elastic embedding

There are two ways to extend the classical continuum mechanics [39, 23, 24, 16, 25]:

Higher-order continua: the number of degrees of freedom is extended. The Cosserat model (also known as micropolar), in which local rotations are added as degrees of freedom, belongs to this family [11]. Timoshenko theory for beams or Reissner-Mindlin theory for plates are examples of higher order continua.

Higher-grade continua: the degrees of freedom are kept identical but higher-order gradients of the displacement field are involved in the elastic energy. Mindlin's Strain-Gradient Elasticity (SGE) model [23, 25, 24] belongs to this family. Euler-Bernoulli theory for beams or Kirchhoff-Love theory for plates are examples of higher-grade continua.

The difference between those two approaches is mainly manifest in dynamics where the first approach allows to produce optical branches, while the other not. For the static applications we are interested in³ there is no obvious reasons for adding new degrees of

³Higher-order continua can find interesting applications for the static description of liquid-crystals [13, 15].

freedom. Hence the second approach will be preferred and followed since it requires, also, less material parameters. In this case, the simplest case of higher-grade continua, that is the Strain-Gradient Elasticity (SGE for now on), is considered. Within this framework, experiments having identical solutions in the classical case but differing within SGE can be conceived. To that aim the following subsections will be devoted to shortly introduce this model.

But before, let us formulate two important remarks:

1. We use generalized continua to describe, in continuum fashion, mechanical behavior in situations where we do not have scale separation. Hence we do not use SGE as a fundamental constitutive law, but rather as an accommodating intermediate to extend, a bit, the validity range of classical homogenization [33];
2. What is investigated here is not the accuracy of SGE, but the insufficiency of Cauchy elasticity. SGE is here regarded as a representative model for higher-grade continua considered as a class of behavior that presents features that can not be described by classical elasticity.

2.2. Strain-gradient elasticity: constitutive equations

Experiments have to be conceived in order to be experimentally feasible. Since the only field that can be directly measured is the displacement one, we decide to performed load-controlled tests that enhance kinematic response, instead of constraining it. Hence SGE [23, 25] is considered here in its compliance form. In this situation the following kinematic quantities:

- the infinitesimal strain tensor: $\underline{\underline{\varepsilon}}$;
- the strain-gradient tensor: $\underline{\underline{\eta}} = \underline{\underline{\varepsilon}} \otimes \underline{\underline{\nabla}}$;

are linear functions (\mathcal{L}) of the symmetric Cauchy stress tensor $\underline{\underline{\sigma}}$ and the hyperstress tensor $\underline{\underline{\tau}}$:

$$\begin{pmatrix} \underline{\underline{\varepsilon}} \\ \underline{\underline{\eta}} \end{pmatrix} = \mathcal{L} \begin{pmatrix} \underline{\underline{\sigma}} \\ \underline{\underline{\tau}} \end{pmatrix}$$

In matrix form the linear constitutive law \mathcal{L} reads:

$$\begin{pmatrix} \underline{\underline{\varepsilon}} \\ \underline{\underline{\eta}} \end{pmatrix} = \begin{pmatrix} \underline{\underline{S}} & \underline{\underline{W}} \\ \underline{\underline{W}}^T & \underline{\underline{V}} \end{pmatrix} \begin{pmatrix} \underline{\underline{\sigma}} \\ \underline{\underline{\tau}} \end{pmatrix} \quad (1)$$

Above,

- $\underline{\underline{S}}$ is the classical fourth-order compliance tensor complying with the following index symmetries:

$$S_{ijklm} = S_{jilm} = S_{jiml} = S_{ijml} = S_{lmij} = S_{mlij} = S_{mlji} = S_{lmji}$$

- $\underline{\underline{W}}$ is the fifth-order coupling compliance (CC) tensor complying with the following index symmetries:

$$W_{ijklm} = W_{jiklm} = W_{jilk m} = W_{ijlkm}$$

- $\underline{\underline{V}}$ is the sixth-order second-order compliance (SOC) tensor complying with the following index symmetries:

$$V_{ijklmn} = V_{jiklmn} = V_{jikmln} = V_{ijkmln} = V_{lmnijk} = V_{mlnijk} = V_{mlnjik} = V_{lmnjik}$$

2.3. Pattern class selection

It can be observed on the matrix form of the constitutive law (1) that the tensor $\underline{\underline{W}}$ induces gradient of strain $\underline{\underline{\eta}}$ from the Cauchy stress $\underline{\underline{\sigma}}$. This coupling is interesting because it allows higher-order effects to be directly read off from the displacement field. This point is illustrated analytically in the case of a 1D rod in the appendix B.

The question is then to determine for which microstructures this coupling is activated. It is a classical result that odd-order tensors vanish for centro-symmetric microstructures [12, 41, 4]. It has been demonstrated in [4] that 14 anisotropic systems exist in the specific situation of bidimensionnal SGE. The detail of each situation is provided in appendix A. It appears that the fifth-order compliance tensor $\underline{\underline{W}}$ is non null in the following systems⁴

$$[G_{\mathcal{L}}^{coupl}] = \{[Id], [Z_2^\pi], [Z_3], [D_3], [Z_5], [D_5]\}$$

which are thus the candidates for choosing the symmetry of the pattern for our sample. The natural idea is to retain the anisotropic system having the minimum number of parameters. But, in 2D, we face the following difficulties:

- $[Z_5]$ and $[D_5]$ -invariances are not compatible with any translational invariance. It is worth noting that a kind of $[Z_5]$ -invariance can be found in quasi-crystallographic tilings such as the Penrose tilings (c.f. Fig.3). In order to have a simple pattern this possibility will be discarded;

⁴Since in 2D, the central inversion is equivalent to a rotation of π , odd-order tensors are null for any pattern having Z_2 as a subgroup of their symmetry group.

- if a material is both $[Z_3]$ (resp. $[D_3]$) and invariant by translation, it is automatically $[Z_6]$ -invariant (resp. $[D_6]$). This restriction can be avoided by using different materials in the pattern (c.f. Fig. 4(a) and Fig. 4(b)). This solution is technically possible, especially with dual-extruders Fused Deposition Modeling machines. In order to ease the specimen manufacturing, ensure the shape accuracy and avoid any potential debonding at the interface between the two constitutive materials, this possibility will be however discarded;

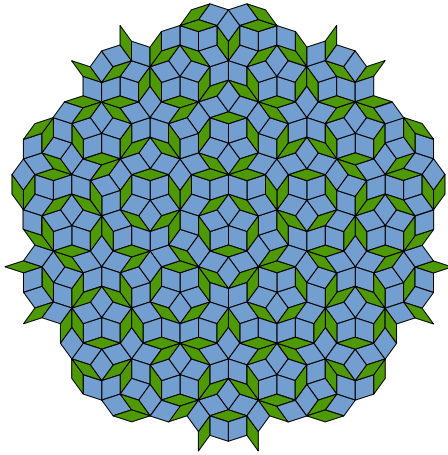
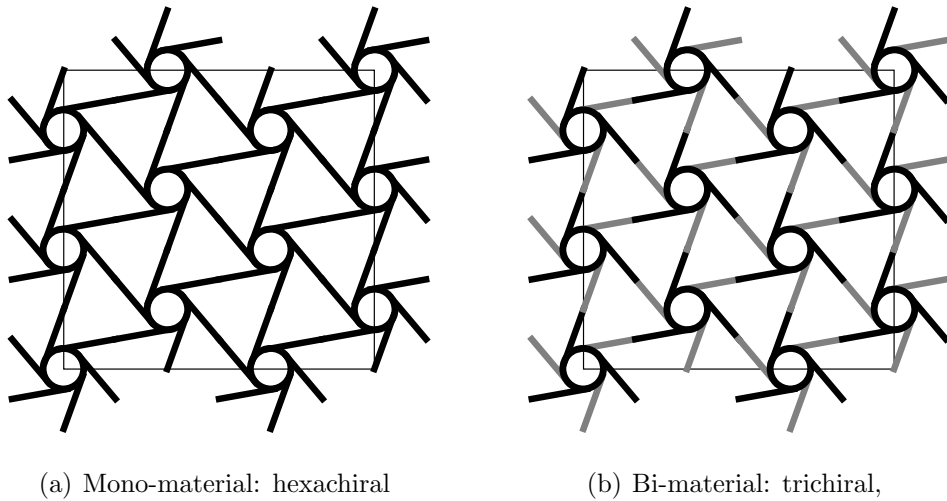


Figure 3: Penrose quasi-crystallographic tiling



(a) Mono-material: hexachiral

(b) Bi-material: trichiral,

Figure 4: Mono- and bi- material patterns, which belong to the $[Z_6]$ and $[Z_3]$ respectively

Hence, in our case, the most simple situation is to consider the $[Z_2^\pi]$ -anisotropy. To evidence the effect due to the lack of centrosymmetry, the same experiment will also be conducted on a material having centrosymmetric architecture. The anisotropic class of

the unit cell of the reference sample will be of type $[D_2]$ and its geometry will be taken similar to the one of the principal sample.

2.4. Particular pattern selection

Finding a $[D_2]$ -architected material among industrial honeycomb standards is easy, but a $[Z_2^\pi]$ one is more challenging. We choose a pattern (Fig. 5(a)) similar to the Flexcore[®] honeycomb produced by Hexcel, which was designed to enable single and compound curvatures of sandwich panels. Based on this pattern⁵, a $[D_2]$ one is proposed (Fig. 5(b)) for the purpose of this study.

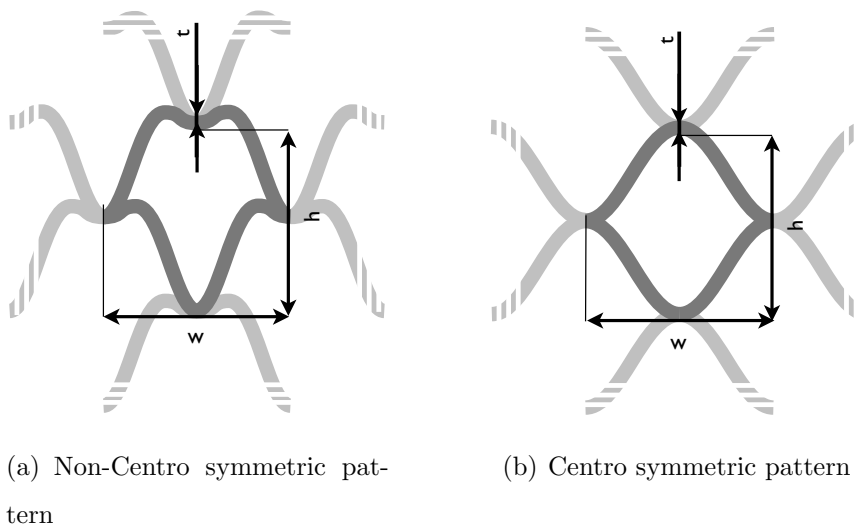


Figure 5: Non-centro and centro-symmetric patterns, which belong to the $[Z_2^\pi]$ and $[D_2]$ respectively. In the figure, w , h and t denote, respectively, the width, the height and the thickness of the pattern.

In order to validate the choice of the patterns some prior FEM computations have been conducted. We consider two specimens made out of 9×8 tiling of the $[Z_2^\pi]$ and $[D_2]$ patterns with $w = 18$ mm, $h = 22$ mm and $t = 2$ mm. For this configuration, the scale separation ratio $\epsilon = m/M = 1/8$. Therefore the inner scale can not be considered infinitely small compared to that of the sample. This point is important since for $\epsilon \rightarrow 0$ classical homogenization result is retrieved with the lost of architected effects [3]

The specimens are submitted to a 1 N uniform tensile force along x axis, as shown Fig. 6. The constitutive material used for numerical simulations is a linear elastic isotropic material, with parameters (Young's modulus $E = 2400$ MPa, Poisson's ratio $\nu = 0.4$)

⁵The curve generating the non centro-symmetric pattern is given by $f(x) = \frac{h}{8} \left(\cos\left(\frac{4\pi x}{w}\right) - 2 \cos\left(\frac{2\pi x}{w}\right) \right)$.

corresponding to solid ABS plastic (*i.e.* not homogenized ABS plastic material obtained by FDM). Computations are performed using Abaqus for CATIA V5 with a mesh size equal to 0.15 mm.

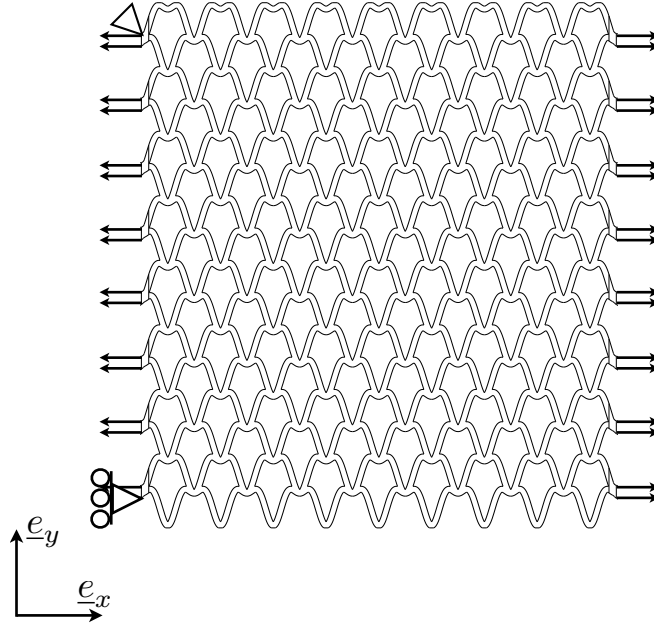


Figure 6: Boundary conditions used for the FEM computation: uniformly distributed tensile force along \underline{e}_x for the left and right ends. Fixed u_x and u_y displacement for the upper left node, fixed u_x for the lower left node to ensure solution unicity.

The resulting deformed geometries for the $[D_2]$ and $[Z_2^\pi]$ architectures are plotted Fig.7(a) & 7(b). The displacement fields for the $[D_2]$ architecture is detailed Fig.8(a) & 8(b) while the same fields for the $[Z_2^\pi]$ architecture are plotted on Fig.9(a) & 9(b):

- For the $[D_2]$ situation the displacement field is classical, the macroscopic strain is homogeneous. The displacement magnitude reveals the low stiffness of the specimen: along \underline{e}_x (resp. \underline{e}_y) the mean displacement at the right end of the specimen (*i.e.* the unconstrained end) is equal to $4.74 \mu\text{m}$ ($2.28 \mu\text{m}$).
- The situation for the $[Z_2^\pi]$ architecture is very different: a flexure-like displacement is superimposed to the elongation. The mean displacement at the right end of the specimen along \underline{e}_x (resp. \underline{e}_y) is equal to $5.59 \mu\text{m}$ (resp. $1.16 \mu\text{m}$), *i.e.* of the same order of magnitude than the corresponding one for the $[D_2]$ situation. The magnitude of the flexure-like heterogeneity is non-negligible: along \underline{e}_x (resp. \underline{e}_y) the difference of displacement at the right end of the specimen is equal to $0.85 \mu\text{m}$ (resp. $1.45 \mu\text{m}$).

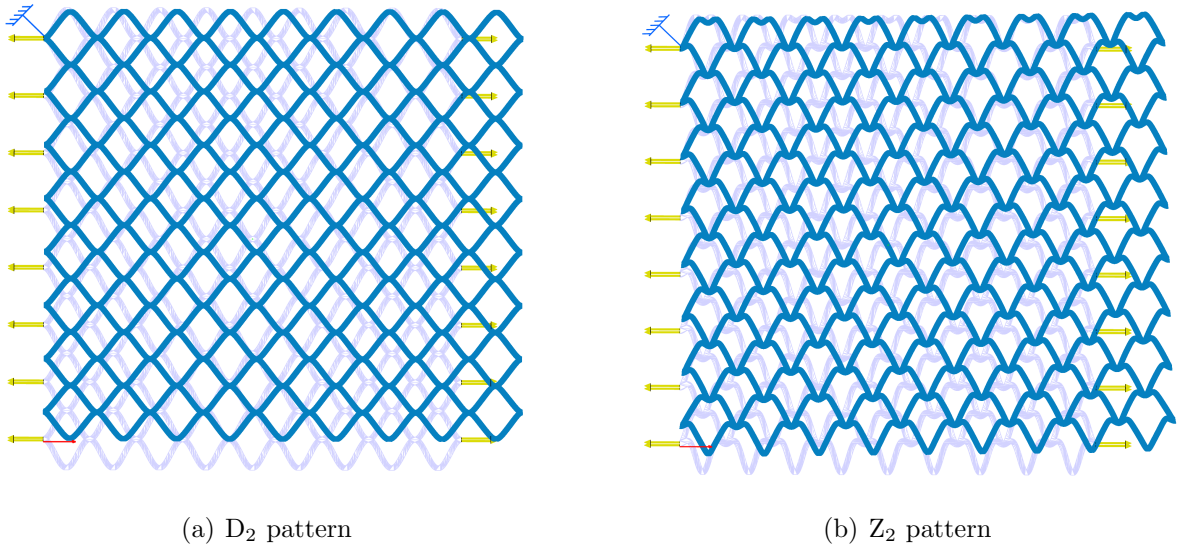


Figure 7: Unloaded (light blue) and deformed geometries (deep blue) under 1 N uniform tensile force along e_x for the centrosymmetric and non centrosymmetric patterns (magnification $\times 5000$).

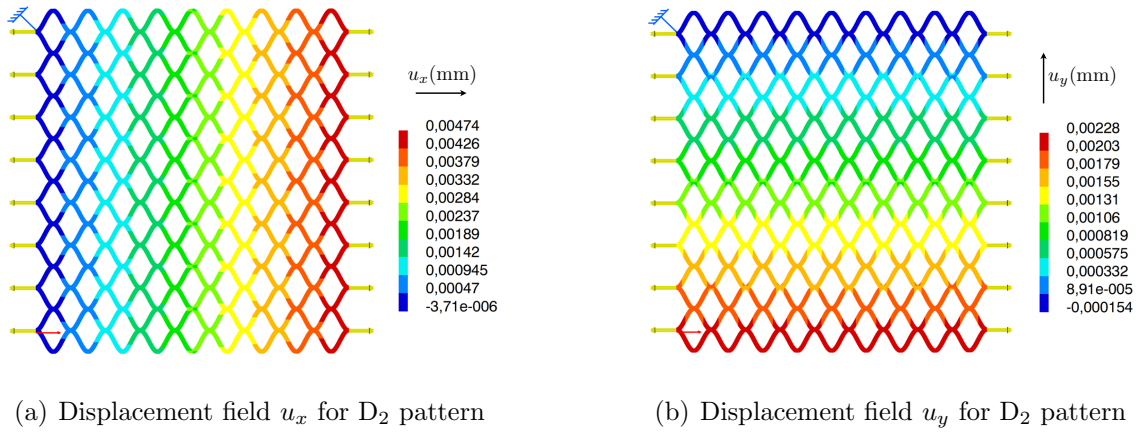


Figure 8: Displacement fields under 1 N uniform tensile force along e_x for the centrosymmetric pattern specimen.

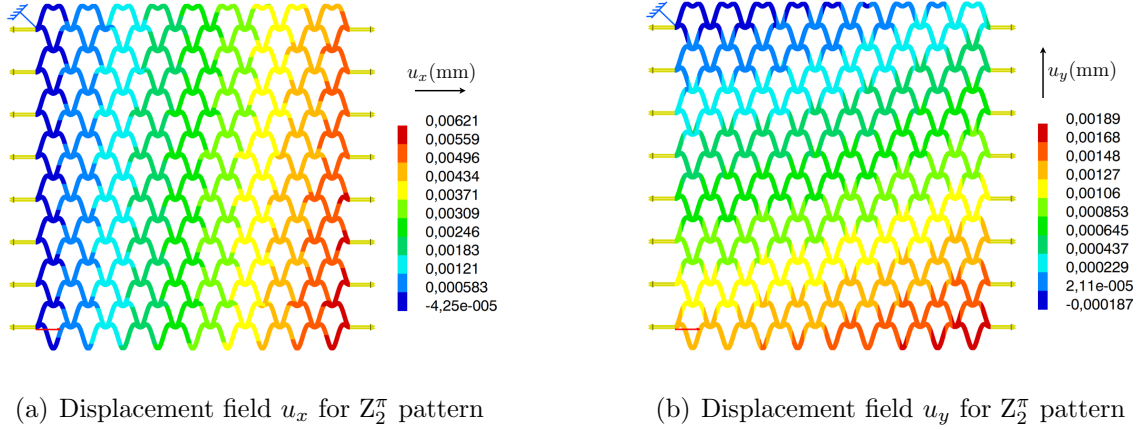


Figure 9: Displacement fields under 1 N uniform tensile force along \underline{e}_x for the non centrosymmetric pattern specimen.

It is thus obvious that in the case of the $[Z_2^\pi]$ architecture, the associated theoretical strain field can not be homogeneous. From a continuum point of view, in the case of classical Cauchy elasticity, such an homogeneous force loading can, of course, not produce an heterogeneous strain field. As discussed before, this situation can, at the opposite, be predicted and explained by higher-gradient theories of elasticity.

These numerical examples advocate for the need of generalized continuum for the overall modeling of architected materials. The question is now to validate this need with respect to real materials and not just numerically. In the experimental case, sources of dispersions are multiple: geometrical defects, material parameters, boundary conditions and mechanical loading... So the question is to check either the higher-order effects evidenced on numerical simulations do emerge in experimental testings or are they not-visible, hidden by the multiple dispersions.

3. Experimental approach

The idea is to propose a test very close to the numerical simulations previously presented. To do so, one has to chose a coherent combination of specimen/RPT/loading setup/measurement technique such that:

1. the specimen enables a distributed load to be applied to its boundaries;
2. the loading setup ensures a uniformly distributed tensile force;
3. the measurement setup allows for a macroscopic analysis of the displacement field.

These three key points will be briefly presented before the obtained results.

3.1. Specimen geometry and manufacturing

First, one wants to choose a usual FDM machine, so that manufacturing defects are representative of the ones obtained with such type of RPT. The Stratasys Dimension SST 768 FDM is selected because it is at the same time an industrial grade device and a rather widespread machine. Due to its stiff frame and good temperature control, this machine is considered to be reliable, allowing dimensional error around 0.1 mm as for several industrial FDM machines [18]. The slice thickness and ABS thread diameter in the present case is 0.254 mm and the production space is equal to $200 \times 200 \times 250$ mm³. The average porosity of the obtained ABS is around 10% [17] and its mechanical properties are slightly anisotropic (e.g. according to [36], the apparent Young's modulus varies around 10% in the plane of manufacturing).

Based on this first choice, the specimen requirements are the following:

- for manufacturing: small enough to fit in the machine, with mesoscale details and wall thickness t large enough to be accurately printed. Specimens out-of-plane thickness must contain several slices;
- for full-field measurement: sufficiently compliant to enable accurate kinematic measurement without requiring large forces, and minimizing the out-of-plane displacement under load;
- for distributed loading : providing fixtures for the loading setup, ensuring no failure in the ends of the specimen.

A specimen satisfying these requirements is presented Fig. 10 (the specimen with the $[D_2]$ -invariant pattern is similar).

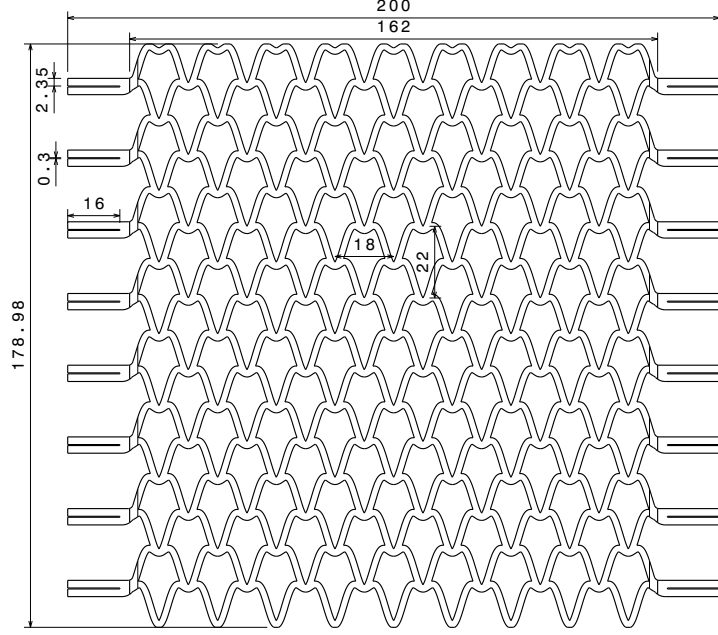


Figure 10: Specimen geometry for $[Z_2^\pi]$ pattern.

The rectangular flat gauge zone is $162 \times 179 \text{ mm}^2$, made of 9×8 cells as in the previous computations. Its out-of-plane thickness is 20 mm corresponding to around 78 slices. The thickness of the walls t is 2 mm so that theoretically up to 7 threads could fit. A tomography of a cell (Fig. 11(a) & 11(b)) shows that only 3 threads are filling the walls in each slice, leaving around 5.5% of unfilled space. It can be observed that the configuration of the threads is inverted with respect to the symmetry axis \underline{e}_y of the cell at each slice. Hence, even if, due to microstructural defects, a slice of matter is not rigorously $[Z_2^\pi]$ -invariant, the global invariance is restored "in average" sense by this out-of-plane alternance. Being only $[Z_2^\pi]$ -invariant in an approximated sense only induced a small, and hence neglectable, perturbation to the result. What is more important is that around 0.8% of the cell section is never filled by any slice. These empty spaces are mainly located in the critical joint area. The resulting material quality being rather poor, an influence on the macroscopic behavior is expected.



Figure 11: Tomographic images of a $[Z_2^\pi]$ cell obtained by FDM, corresponding to two successive slices of the process. The $1048 \times 1223 \times 1121$ voxels images are obtained with the LMT X-ray lab-CT.

The onset of plasticity has been roughly assessed with an FEM simulation considering a solid material instead of the real porous one. It happens at around 500 N if one considers a 17 MPa elastic limit. The computation gives a corresponding average extension along \underline{e}_x axis equal to 2.5 mm, while the heterogeneity of extension along \underline{e}_y axis is around 0.345 mm. Such supposed displacement fields are compatible with standard full-field measurements and cameras. A global Digital Image Correlation (DIC)[5] procedure enables a measurement uncertainty around a centipixel [20], *i.e.* lower than the sought displacement heterogeneity.

The gauge zone is completed by a series of clamps at each lateral ends. They are 40 mm-thick to transmit load from setup to gauge zone without breaking. For each clamps, two M4 bolts with washers will be used to grip the loading setup.

3.2. Loading setup

The loading setup is simple even though very rare for material testing. It is based on a steel whippletree distributing the main force to several points by use of geometrical relationship (Fig. 12). To the author's knowledge the first appearance of such mechanism was during the 12th century for horse or ox carriages [40]. This principle is used in mechanical testing for decades (*e.g.* for aircraft's wing testing), but nearly never used in the case of material testing (a rare counterexample is [30]).

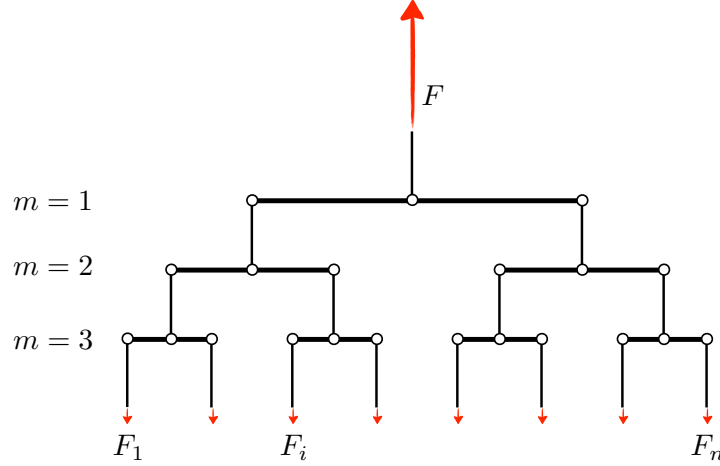


Figure 12: Used linkage tree configuration with the 8 boundary conditions F_n for the designed sample.

It combines several features:

- it does not constrain the specimen to any transverse displacement. This problem of unwanted displacement induced by clamping the specimen has already been addressed by [26], who concludes that transmitting the load through a slitted end (*i.e.* parallel beams), has to be preferred;
- it does not constrain the specimen to any displacement along the loading axis, only a distributed load is applied. This enables for example free rotation of the ends (or even more complex motions), which is necessary for anisotropic material studies where a homogeneous gauge zone is sought [6];
- last, it distributes the load in a predefined manner on every clamping points, such that there is a proportional relationship between each clamping point force F_i and the main force F . It is distributed equally in the present case, but nearly any possibilities exist because of a continuous adaptable setting of the geometric parameters (even with $n \neq 2^m$ with m the number of tree stage). Considering small displacements, that means that as soon as any F_i is equal to zero (because of specimen local failure or clamp failure), every other F_i are equal to zero because of the force balance of the linkage.

The whippetree linkages are 200 mm long for each stage, to ensure that the reorientation of the applied forces due to the specimen lateral strain under load is negligible. A whippetree is fixed to each end of the specimen. One is related to a fix part and the other to

a 100 kN servo-hydraulic actuator equipped with a 500 N load cell. The complete setup is around 1800 mm. Consequently, to avoid any out-of-plane bending due to the setup own weight, the specimen and the whippetree are sliding on a horizontal plate.

3.3. Measurement protocol

The goal of the experiment being to differentiate a Cauchy elasticity behaviour from a more complex one, a full-field kinematic measurement is mandatory.

Since the lattice has thin walls (around a tenth of the cell size, and a hundredth of the specimen size), there is a relatively small area to carry kinematic informations over the wall width t . Two procedures of the Image Correlation techniques family could be of interest. Roughly speaking, these are full-field measurement methods that characterizes quantitatively [20] the displacement on the surface of a sample by comparing a deformed image of it to a reference one. A first method, called Virtual Image Correlation (VIC) technique⁶ [37], is dedicated to very thin ‘objects’ (wires, liquid interfaces ...), but displacement along the main axis of these objects is not obtained. A second method, nowadays well-known in the experimental mechanics field, is the Digital Image Correlation (DIC) [35]. Contrary to the previous one, it relies on two measured images. With global-DIC [5], the motion is directly captured on a finite element mesh that enables a dialogue between measured results and simulation. In the present case where the walls are thin, it however requires high resolution images or a tailored kinematics (such as a beam theory DIC [21], that could be here extended to a lattice one).

One proposes to circumvent this difficulty by ‘spreading’ the kinematic informations from the walls to the void of the cell. To this aim a speckled sheet of elastomer (dental dam by 4D Rubber®) is stretched and glued to the gauge zone (Fig. 13). Because of the low Young’s modulus (1.3 MPa) of the elastomer sheet and its small thickness (0.2 mm) in comparison with the gauge zone, a weak coupling occurs: the specimen imposes its displacement to the sheet without being constrained by the stiffness of the latter. One takes care to apply a small initial tension so that the elastomer sheet is prevented from buckling under low magnitude compression.

One will use both a global (for measuring the displacement field without any a priori knowledge except continuity) and, for measuring Cauchy elasticity kinematic, an Inte-

⁶Briefly speaking, it consists in the comparison between the object silhouette and a theoretical one.

grated DIC techniques [34]. With this last technique the searched kinematic is expressed on a model basis (generally composed of very few parameters compared with global DIC). It allows models to be identified and discriminated and can be applied for the (in)validation of Cauchy elasticity.

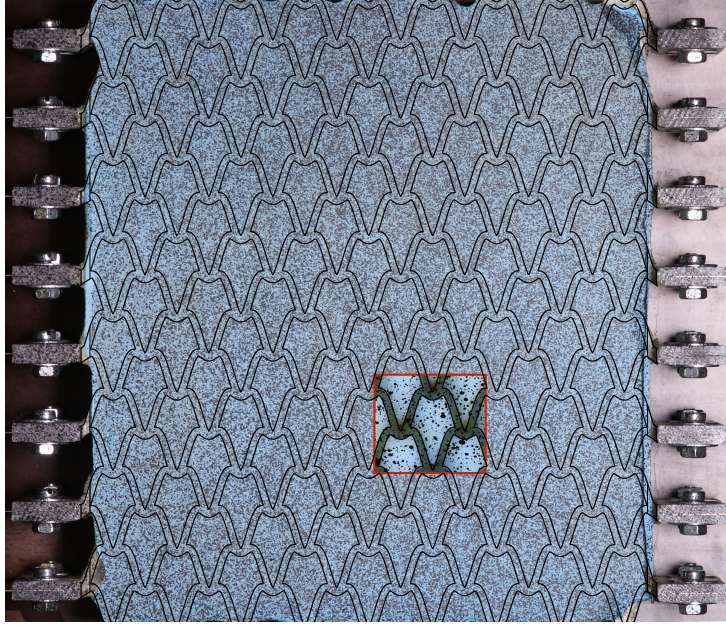


Figure 13: Illustration of the measurement principle: specimen clamps (gray parts with bolts) are visible on both sides, rubber sheet (light blue) is over the gauge zone. For clarity purpose, the theoretical geometry of the specimen (black lines) and an image obtained by backlighting (red-line surround) are presented.

A series of displacement-controlled loading-unloading is applied to each specimen, up to around 500 N in order to stay in the elastic regime. First loading-unloading is done for setup self-alignment, second and third to verify the repeatability. Images are at different steps of actuator displacement. The camera is a DSLR one (Canon 60D, 5184×3456 pix.) equipped with a 105-mm fixed focal lens, leading to a physical pixel size equal to $65.5 \mu\text{m}$.

Images at maximum load and mid-load are then post-processed (mid-load images are used instead of minimum load since they ensure that the specimen is already well aligned and that the load is well distributed). The Correli 3.0 DIC algorithm [22] is used to perform the measurement computation. It relies on the registration of an image $f(\underline{x})$, defined for every pixels of the selected region of interest \underline{x} in the reference configuration and a series of pictures $g(\underline{x})$ in the deformed configurations. The registration operation consists of minimizing the sum of squared differences between the deformed image corrected for

its displacement and the reference image. Hence

$$u(\underline{x}) = \text{Arg} \min_{u \in E} \sum_{\underline{x}} (f(\underline{x}) - g(\underline{x} + u(\underline{x})))^2 \quad (2)$$

with E , a subspace composed of a predefined and constrained kinematic basis. For a global DIC procedure [5], rich in degrees of freedom, the basis can be chosen as a finite element mesh kinematic, using standard shape functions. For an integrated approach [34], the displacement field is constrained by a model. It is proposed here a kinematic basis composed of 6 displacement fields:

- rigid body motion: translations along \underline{e}_x and \underline{e}_y , and rotation along \underline{e}_z ,
- Cauchy elasticity solution for a homogeneous test: displacement fields from uniform tensile strains ε_{xx} and ε_{yy} , and uniform shear strain ε_{xy} .

It can be noted that a material that does not follow the Cauchy elasticity model would not be completely corrected by the previous chosen basis. Hence a difference between the constrained fields (integrated) and the global one would not be composed only of noise and would highlight the failure of the Cauchy elasticity model.

3.4. Results

One subtracts the rigid body motion to the displacement field obtained by a global DIC algorithm for an easier appreciation of the field fluctuations. The used DIC mesh is much finer than the cell size (*i.e.* the kinematics is only constrained to a FEM-like field, not a homogeneous Cauchy elasticity one). It can be noted that with the global DIC procedure, the gray level residual field at convergence is very low (<0.1% of the dynamic range of the images) meaning that all the kinematic has been correctly captured. The obtained total displacement fields u^{Mes} are presented Fig. 14(a) & 14(b), with the colorbar corresponding to u_x^{Mes} . As a first sight, $[D_2]$ and $[Z_2^\pi]$ fields are close to the classical Cauchy elasticity solution: homogeneous strain along both \underline{e}_x and \underline{e}_y directions. The fluctuations at the mesoscale are not visible. At first sight, the distributions of u_x^{Mes} are flat, corresponding to a uniform tensile loading applied to homogeneous specimens.

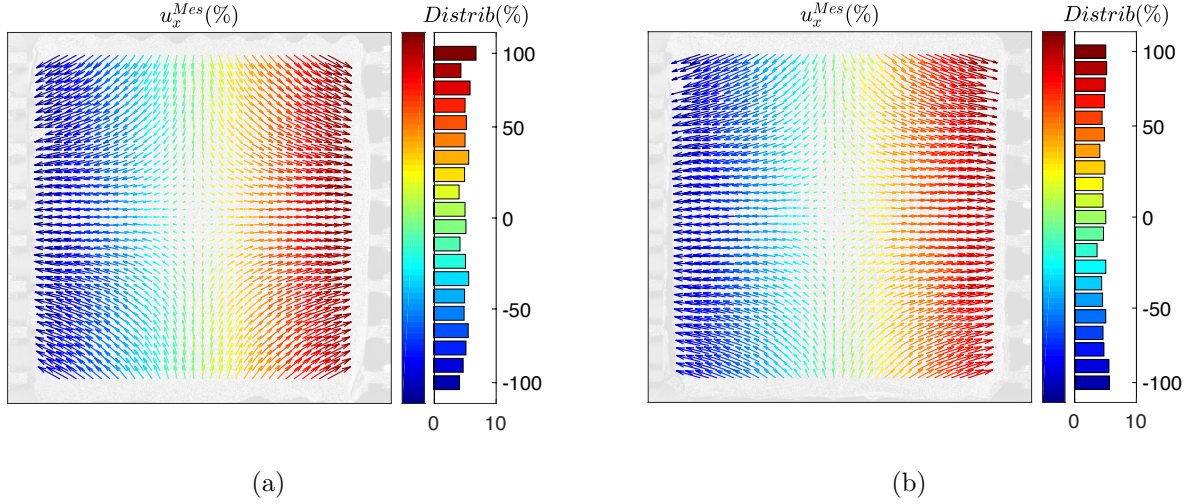


Figure 14: Total displacement field (without the rigid body motion) for (a) the $[D_2]$ and (b) the $[Z_2^\pi]$ geometry.

Looking for the ‘compliance coefficients’ *i.e.* the ratios of homogeneous strains ε_{xx} , ε_{yy} and ε_{xy} to the applied force F , one first verify that the experimental discrepancies are small. To this aim several setup modifications (turning the specimen, adjusting the whippetree) are operated. The optical distortions (whose influence have been estimated by moving the specimens with the same maximum magnitude as during a test, but without load) and the effect of load cycling are also assessed. Results shown Fig. 15 prove that the discrepancies are low in comparison with the average measured values.

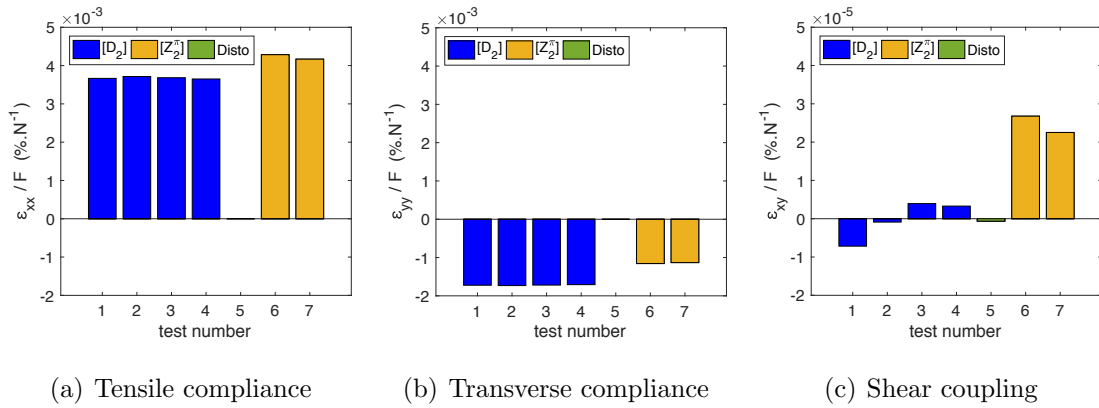


Figure 15: Compliance coefficients for $[D_2]$ and $[Z_2^\pi]$ architectures. Different test conditions are presented: for the $[D_2]$ architecture, test number 1 is with specimen in initial position, number 2 with specimen in-plane flipped, 3 back in initial position and a finer adjustment of the whippetree and 4 after the addition of 15 load cycles. Number 5 corresponds to an estimation of the distortions influence. For the $[Z_2^\pi]$ architecture, test number 6 is in initial position and 7 after 1 cycle.

The compliance coefficients obtained with the final setup configuration are presented

Tab. 1. Compliances are the average of 2 successive measures, and error ranges are calculated as the difference between the 2 values, thus including all experimental discrepancies.

	ε_{xx}/F $[10^{-6}.N^{-1}]$	ε_{yy}/F $[10^{-6}.N^{-1}]$	ε_{xy}/F $[10^{-6}.N^{-1}]$
$[D_2]$	36.66 ± 0.17	-17.14 ± 0.05	0.03 ± 0.00
$[Z_2^\pi]$	42.26 ± 0.59	-11.44 ± 0.13	0.24 ± 0.021

Table 1: Measured compliance coefficients. Ranges are evaluated by repeating the measurement.

Several points are worth noting:

- First the order of magnitude is coherent with the ones obtained by simulation, given in Table 2. Measured compliances are on average more important, which is expected because of the porosity of the sample described in Section 3.1. Simulations were indeed performed using a isotropic elastic model and a molded ABS Young modulus value (2400 MPa) while FDM ABS is reported to be slightly anisotropic in the 3D-printer plane and having a lower average Young modulus (*e.g* [10] measures values around 1990 MPa, *i.e.* 17% lower than the used value). In the present case, the stiffness is expected to be even lower because of the narrow walls (2-mm width) of the specimens not allowing an ABS density as high as for the standard tensile specimens used by [10] (6-mm width).
- Second, $[D_2]$ and $[Z_2^\pi]$ measured specimen Cauchy compliances are roughly alike since the geometries are not very different (same wall thickness to cell size ratio, quadrangular lattice, etc.). FEM results were alike.
- Last, an unexpected shear strain appears under tension in the $[D_2]$ case, however very small (3 order of magnitude below the tensile strains). It may be due to specimen or setup flaws. For the $[Z_2^\pi]$ specimen, on the contrary, this non-null compliance is predicted, however lower than the FEM value. This could be due to the setup own stiffness or friction with the supporting plate.

	ε_{xx}/F $[10^{-6}.N^{-1}]$	ε_{yy}/F $[10^{-6}.N^{-1}]$	ε_{xy}/F $[10^{-6}.N^{-1}]$
$[D_2]$	29.25	-12.73	0
$[Z_2^\pi]$	34.50	-8.11	0.94

Table 2: Compliance coefficients obtained from FEM.

The key point of this study is now to check whether the Cauchy elasticity is sufficient to describe the 2 types of specimen behaviour. To do so, one now calculates the relative difference between the Cauchy elastic fields obtained with Integrated-DIC u^{Cauchy} and the measured displacement field (without RBM) u^{Mes} . Fig. 16(a) & 16(b) (resp. Fig. 17(a) & 17(b)) show the result, with the colorbar corresponding to the component along \underline{e}_x (resp. \underline{e}_y). In the case of the $[D_2]$ geometry, this difference is composed of displacement noise without spatial coherency and expected mesoscale pattern. A light long wave pattern is visible along the \underline{e}_x direction (Fig. 16(a)), probably due to a setup or specimen defect. For $[Z_2^\pi]$ geometry, the kinematic field shows no noticeable pattern along \underline{e}_y (Fig. 17(b)) but has a non-negligible extra component, up to 13 % of the measured displacement magnitude along \underline{e}_x (Fig. 16(b)). This one is not limited to the end regions of the specimen and is thus not just a boundary effect. The distribution of values for the $[Z_2^\pi]$ geometry is more extended than for the $[D_2]$ one, clearly underlining the existence of a different kinematic field. One deduces from the analysis of the experimental displacement fields that, roughly speaking, a rotation of the left and right ends, appears. Such a kinematics is unpredicted by Cauchy elasticity. It is similar to a bending kinematics (Fig. 18), but contrary to the usual bending of a beam where the transverse displacement along \underline{e}_y is ‘amplified’ by the length of the specimen, here its shortness leads to an nearly invisible transverse displacement, while the normal displacement along \underline{e}_x is remarkable.

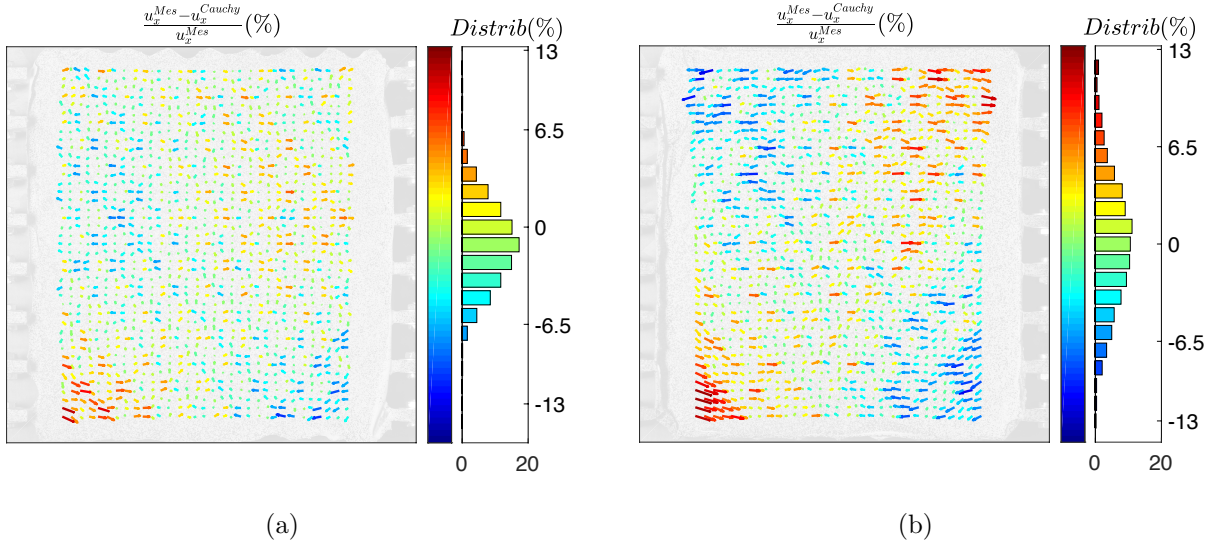


Figure 16: Relative residual displacement field (*i.e.* not captured by the Cauchy elasticity) for (a) the $[D_2]$ and (b) the $[Z_2^\pi]$ geometry. The colorbar and the histogram correspond to the \underline{e}_x component.

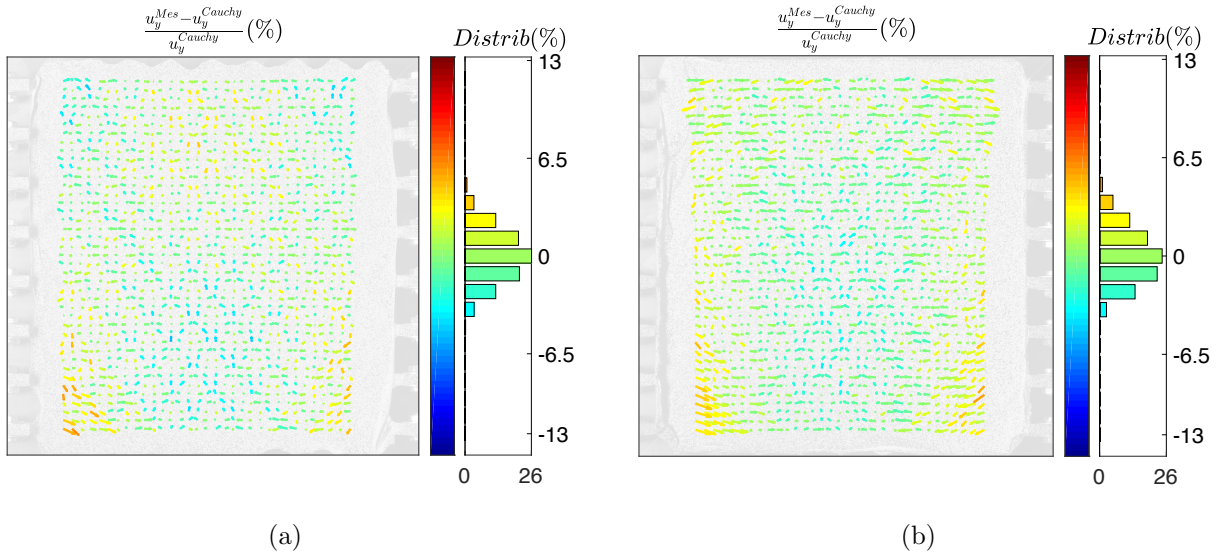


Figure 17: Relative residual displacement field (*i.e.* not captured by the Cauchy elasticity) for (a) the $[D_2]$ and (b) the $[Z_2^\pi]$ geometry. The colorbar and the histogram correspond to the \underline{e}_y component.

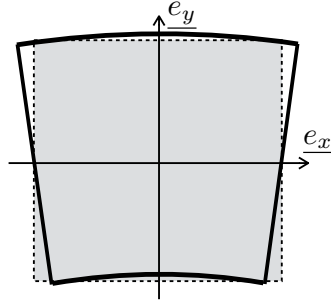


Figure 18: Schematic representation of the deformation observed on the $[Z_2^\pi]$ geometry. Dotted line = initial state, thick line = deformed state.

4. Conclusion

The overall elastic behavior of architected materials is generally described by the mean of the classical Cauchy continuum. In this paper a situation for which this procedure fail to adequately described the observed phenomenon has been identified in the case of quasi-static loadings. This situation is related to non-standard couplings that occur for materials having a non-centrosymmetric architecture.

This departure from Cauchy elasticity has been experimentally observed on a uniaxial tension test on a non-centro-symmetric lattice. To assess that the effect is related to architecture, the same experiment has also been conducted on a centro-symmetric lattice where the non-standard coupling should not produce. The quality of the experiment has been investigated and assessed, ensuring that the measured higher-gradient are not noise and are, hence, characteristic of the mechanical behavior of the architected material.

The conclusion is that an overall description of this experiment can not be achieved in the realm of classical Cauchy elasticity. The idea that these higher-gradient effects, noticeable on computations, would vanish when considering a real case with manufacturing defects turns out to be wrong. It should be pointed that this doesn't validate the used strain-gradient elasticity which only serve a conceptual intermediate to conceive the experiment. Using the same test, an enrichment of the kinematic basis with second gradient fields for the full field measurement would able model (in)validation, but it was not in the scope of the present paper.

Acknowledgements

The authors would like to gratefully acknowledge G. Rosi, J. Dirrenberger and A. Lebéé for their discussions and the Fédération Francilienne de Mécanique for financial support through its starting grant program. The LMT CT scans have been performed from the support of the French “Agence Nationale de la Recherche” through the “Investissements d’avenir” Program under the reference “ANR-10-EQPX-37 MATMECA”. The authors would like to thanks the two reviewers for their careful reading and their constructive comments and questions.

Appendix

A. Symmetry classes

It is known since the mid 90’ that the space of 2D elasticity tensors is divided into 4 anisotropic classes. Those classes are reported together with their number of independent components in the following table:

Name	Digonal	Orthotropic	Tetragonal	Isotropic
$[G_{\mathcal{L}}]$	$[Z_2]$	$[D_2]$	$[D_4]$	$[O(2)]$
$\#_{\text{indep}}(\mathcal{L})$	6 (5)	4	3	2

Table A1: The names, the sets of subgroups $[G_{\mathcal{L}}]$ and the numbers of independent components $\#_{\text{indep}}(\mathcal{L})$ for the 4 symmetry classes of \mathcal{L} . The in-parenthesis number indicates the minimal number of components of the law in an appropriate basis.

It can be observed that, for classical elasticity, the situation is relatively simple, with few anisotropic systems. Extending classical elasticity to strain-gradient elasticity the number of anisotropic system increases by far. To be more specific, it has been demonstrated that there exists 14 anisotropic systems, which are reported in the following table:

Name	Oblique	Rectangular	Digonal	Orthotropic	Trichiral	Trigonal	Tetrachiral	Tetragonal
$[G_{\mathcal{L}}]$	[Id]	$[Z_2^\pi]$	$[Z_2]$	$[D_2]$	$[Z_3]$	$[D_3]$	$[Z_4]$	$[D_4]$
$\#\text{indep}(\mathcal{L})$	45 (44)	27	36 (35)	16	15 (14)	10	13 (12)	9
Name	Pentachiral	Pentagonal	Hexachiral	Hexagonal	Hemitropic	Isotropic		
$[G_{\mathcal{L}}]$	$[Z_5]$	$[D_5]$	$[Z_6]$	$[D_6]$	$[\text{SO}(2)]$	$[\text{O}(2)]$		
$\#\text{indep}(\mathcal{L})$	9 (8)	7	9 (8)	7	7	6		

Table A2: The names, the sets of subgroups $[G_{\mathcal{L}}]$ and the numbers of independent components $\#\text{indep}(\mathcal{L})$ for the 14 symmetry classes of \mathcal{L} . The in-parenthesis number indicates the minimal number of components of the law in an appropriate basis.

The detail of each situation is provided here after, where the classical elasticity is retrieved by restraining the complete operator to only its \mathbf{C} part:

$$\mathcal{L}_{\text{Id}} = \begin{pmatrix} \mathbf{C} & \mathbf{M} \\ \approx_{Z_2} & \approx_{\text{Id}} \\ \mathbf{M}^T & \mathbf{A} \\ \approx_{\text{Id}} & \approx_{Z_2} \end{pmatrix} ; \quad \mathcal{L}_{Z_2^\pi} = \begin{pmatrix} \mathbf{C} & \mathbf{M} \\ \approx_{Z_2} & \approx_{Z_2^\pi} \\ \mathbf{M}^T & \mathbf{A} \\ \approx_{Z_2^\pi} & \approx_{Z_2} \end{pmatrix} \quad (\text{A1})$$

$$\mathcal{L}_{Z_2} = \begin{pmatrix} \mathbf{C} & 0 \\ \approx_{Z_2} & \\ 0 & \mathbf{A} \\ & \approx_{Z_2} \end{pmatrix} ; \quad \mathcal{L}_{D_2} = \begin{pmatrix} \mathbf{C} & 0 \\ \approx_{D_2} & \\ 0 & \mathbf{A} \\ & \approx_{D_2} \end{pmatrix} \quad (\text{A2})$$

$$\mathcal{L}_{Z_3} = \begin{pmatrix} \mathbf{C} & \mathbf{M} \\ \approx_{\text{O}(2)} & \approx_{Z_3} \\ \mathbf{M}^T & \mathbf{A} \\ \approx_{Z_3} & \approx_{Z_6} \end{pmatrix} ; \quad \mathcal{L}_{D_3} = \begin{pmatrix} \mathbf{C} & \mathbf{M} \\ \approx_{\text{O}(2)} & \approx_{D_3} \\ \mathbf{M}^T & \mathbf{A} \\ \approx_{D_3} & \approx_{D_6} \end{pmatrix} \quad (\text{A3})$$

$$\mathcal{L}_{Z_4} = \begin{pmatrix} \mathbf{C} & 0 \\ \approx_{D_4} & \\ 0 & \mathbf{A} \\ & \approx_{Z_4} \end{pmatrix} ; \quad \mathcal{L}_{D_4} = \begin{pmatrix} \mathbf{C} & 0 \\ \approx_{D_4} & \\ 0 & \mathbf{A} \\ & \approx_{D_4} \end{pmatrix} \quad (\text{A4})$$

$$\mathcal{L}_{Z_5} = \begin{pmatrix} \mathbf{C} & \mathbf{M} \\ \approx_{\text{O}(2)} & \approx_{D_5} \\ \mathbf{M}^T & \mathbf{A} \\ \approx_{D_5} & \approx_{\text{SO}(2)} \end{pmatrix} ; \quad \mathcal{L}_{D_5} = \begin{pmatrix} \mathbf{C} & \mathbf{M} \\ \approx_{\text{O}(2)} & \approx_{D_5} \\ \mathbf{M}^T & \mathbf{A} \\ \approx_{D_5} & \approx_{\text{O}(2)} \end{pmatrix} \quad (\text{A5})$$

$$\mathcal{L}_{Z_6} = \begin{pmatrix} \mathbf{C} & 0 \\ \approx_{\text{O}(2)} & \\ 0 & \mathbf{A} \\ & \approx_{Z_6} \end{pmatrix} ; \quad \mathcal{L}_{D_6} = \begin{pmatrix} \mathbf{C} & 0 \\ \approx_{\text{O}(2)} & \\ 0 & \mathbf{A} \\ & \approx_{D_6} \end{pmatrix} \quad (\text{A6})$$

$$\mathcal{L}_{\text{SO}(2)} = \begin{pmatrix} \mathbf{C} & 0 \\ \approx_{\text{O}(2)} & \\ 0 & \mathbf{A} \\ & \approx_{\text{SO}(2)} \end{pmatrix} ; \quad \mathcal{L}_{\text{O}(2)} = \begin{pmatrix} \mathbf{C} & 0 \\ \approx_{\text{O}(2)} & \\ 0 & \mathbf{A} \\ & \approx_{\text{O}(2)} \end{pmatrix} \quad (\text{A7})$$

The link between generalized compliance tensors and generalized rigidity ones are

provided by the following relation:

$$\underset{\cong}{\mathbb{S}} = \underset{\cong}{\mathbb{C}}^{-1} + \underset{\cong}{\mathbb{C}}^{-1} : \underset{\cong}{\mathbb{M}} : \underset{\cong}{\mathbb{M}}^{-1} : \underset{\cong}{\mathbb{M}}^T : \underset{\cong}{\mathbb{C}}^{-1} \quad ; \quad \underset{\cong}{\mathbb{W}} = -\underset{\cong}{\mathbb{C}}^{-1} : \underset{\cong}{\mathbb{M}} : \underset{\cong}{\mathbb{M}}^{-1} \quad ; \quad \underset{\cong}{\mathbb{V}} = \underset{\cong}{\mathbb{M}}^{-1}$$

with

$$\underset{\cong}{\mathbb{M}} = \underset{\cong}{\mathbb{A}} - \underset{\cong}{\mathbb{M}}^T : \underset{\cong}{\mathbb{C}}^{-1} : \underset{\cong}{\mathbb{M}}$$

It can be observed that in the case $\underset{\cong}{\mathbb{M}} = 0$, this simplifies to

$$\underset{\cong}{\mathbb{S}} = \underset{\cong}{\mathbb{C}}^{-1} \quad ; \quad \underset{\cong}{\mathbb{W}} = \underset{\cong}{\mathbb{0}} \quad ; \quad \underset{\cong}{\mathbb{V}} = \underset{\cong}{\mathbb{A}}^{-1}$$

B. 1D analytic solution

B1. Equilibrium equations: general case

In strain-gradient elasticity the linear momentum reads [23, 14]:

$$\text{Div} \underset{\sim}{\mathbb{s}} + \underset{\sim}{\mathbb{f}} = 0$$

where $\underset{\sim}{\mathbb{s}}$ is the effective second order symmetric stress tensor, defined as follows:

$$\underset{\sim}{\mathbb{s}} = \underset{\sim}{\sigma} - \text{Div} \underset{\simeq}{\tau}$$

Hence the stress quantities that appears in the equilibrium is a combination of the Cauchy stress tensor $\underset{\sim}{\sigma}$ and the hyperstress tensor $\underset{\simeq}{\tau}$.

Bulk equations are supplemented with the Neumann Boundary Conditions (B.C.) on surface

$$\begin{cases} t_i = s_{ij}n_j - P_{ml}(P_{mj}\tau_{ijk}n_k),l \\ R_i = \tau_{ijk}n_jn_k \end{cases} \quad (\text{B1})$$

where the quantities \underline{t} , \underline{R} , and \underline{n} are respectively, the traction (i.e. a force per unit area), the double-force per unit area and the outward normal. The quantity \underline{P} , which is the projector onto the tangent plane, is defined as follows:

$$\underline{P} = \underline{I} - \underline{n} \otimes \underline{n}$$

It worth being noted that if the boundary of the domain is not smooth boundary conditions should be added on edges (in 3D) or at the corners of the domain in 2D. These conditions will not be detailed here.

B2. 1D tension test

In a pure 1D setting, the constitutive law is given by 3 scalars⁷:

$$\begin{pmatrix} \sigma \\ \tau \end{pmatrix} = \begin{pmatrix} c & m \\ m & a \end{pmatrix} \begin{pmatrix} \varepsilon = u' \\ \eta = u'' \end{pmatrix}$$

As illustrated on Fig. 1(a) and 1(b) in 1D the constitutive law can be "isotropic" if $m = 0$, or hemitropic (the only 1D "anisotropic" situation) if $m \neq 0$.



Figure B1: In 1D composite materials can either be (a) centro-symmetric unit cell (isotropic) or (b) non-centro-symmetric unite cell (hemitropic).

To build a bridge with the main part of the text, consider the Z_2^π -invariant pattern previously studied and build two different kind of beam from it. Obtained beams are depicted on figures 2(a) and 2(b), the first is isotropic 1D ($m = 0$), while the second is hemitropic 1D ($m \neq 0$).

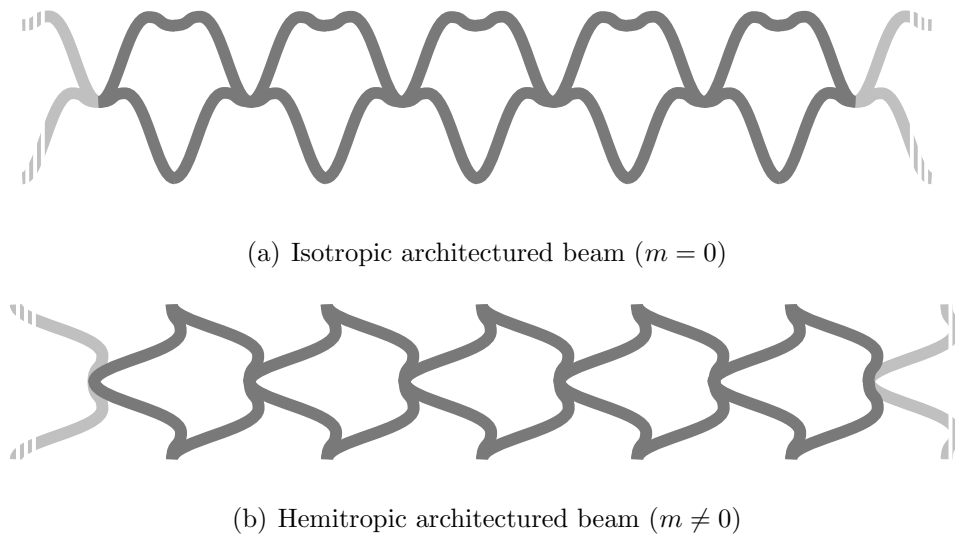


Figure B2: Architected beams made from the Z_2^π -invariant pattern.

It should be noted that the uniaxial hemitropic situation studied here after, illustrated on 2(b), differs from the situation studied in the main part of the text. Indeed, it is in 1D the only situation producing a non-trivial coupling, the situation 2D is, as illustrated in main part, much richer.

⁷In 1D those quantities have the following units $c : [N]$, $m : [N][m]$ and $a : [N][m]^2$.

The elastic energy reads in this case:

$$2\mathcal{W} = \sigma\varepsilon + \tau\eta = c(u')^2 + 2mu'u'' + a(u'')^2$$

This energy is positive definite provided the relation $ac - m^2 \geq 0$ is verified. Positiveness of the classical elasticity is assumed, and hence $a \geq 0$.

In this case the equivalent stress reduces to $s = \sigma - \tau'$ and, in absence of body force, the equilibrium equation $s' = 0$ becomes:

$$\sigma' - \tau'' = 0$$

Inserting the constitutive law, the following 4th order ODE is obtained:

$$cu'' - au^{(4)} = 0$$

the general solution of which is

$$u(x) = \lambda^2 (C_1 e^{\frac{x}{\lambda}} + C_2 e^{-\frac{x}{\lambda}}) + C_3 x + C_4$$

This solution depends on a through the quantity $\lambda = \sqrt{\frac{a}{c}}$ which is homogeneous to a length. λ is a characteristic length of the problem.

The two following points can be noted:

1. The equilibrium equation does not involved the parameter m . Its influence can only be felt through boundary conditions;
2. The displacement field is polynomial if either c or a is null. If a vanishes a general linear displacement field is obtained, while is cubic if c vanishes.

The constants have to be determined from the boundary conditions. At the boundaries the force is imposed to F while the hyper force is null. The problem is of Neumann type so the constant C_4 is not imposed by the B.C.. Without loss of generality, C_4 can be set to 0. For the other B.C. the expressions of σ and τ need to be computed. Beforehand let's determine ε and η , from the expression of the displacement field:

$$\varepsilon = \lambda(C_1 e^{\frac{x}{\lambda}} + C_2 e^{-\frac{x}{\lambda}}) + C_3 \quad ; \quad \eta = C_1 e^{\frac{x}{\lambda}} + C_2 e^{-\frac{x}{\lambda}}$$

and using the constitutive law we obtain

$$\begin{aligned} \sigma &= C_1(m + c\lambda)e^{\frac{x}{\lambda}} + C_2(m - c\lambda)e^{-\frac{x}{\lambda}} + cC_3 \\ \tau &= C_1(a + m\lambda)e^{\frac{x}{\lambda}} + C_2(a - m\lambda)e^{-\frac{x}{\lambda}} + mC_3 \end{aligned}$$

As a consequence:

$$s = \sigma - \tau' = cC_3$$

For the tensile loading we have, on the right boundary:

$$\begin{aligned} t\left(\frac{L}{2}\right) &= s\left(\frac{L}{2}\right) = \sigma\left(\frac{L}{2}\right) - \tau'\left(\frac{L}{2}\right) = cC_3 = F \\ R\left(\frac{L}{2}\right) &= C_1(a + m\lambda)e^{\frac{L}{2\lambda}} + C_2(a - m\lambda)e^{-\frac{L}{2\lambda}} + mC_3 = 0 \end{aligned}$$

while on the left boundary:

$$\begin{aligned} t\left(-\frac{L}{2}\right) &= -s\left(-\frac{L}{2}\right) = -\sigma\left(-\frac{L}{2}\right) - \tau'\left(-\frac{L}{2}\right) = -cC_3 = -F \\ R\left(-\frac{L}{2}\right) &= C_1(a + m\lambda)e^{-\frac{L}{2\lambda}} + C_2(a - m\lambda)e^{\frac{L}{2\lambda}} + mC_3 = 0 \end{aligned}$$

Leading to

$$C_1 = -\frac{Fme^{\frac{L}{2\lambda}}}{c\lambda(e^{L/\lambda} + 1)(c\lambda + m)} \quad ; \quad C_2 = -\frac{Fme^{\frac{L}{2\lambda}}}{c\lambda(e^{L/\lambda} + 1)(c\lambda - m)} \quad ; \quad C_3 = \frac{F}{c}$$

The displacement field have the following expression:

$$u(x) = \frac{F}{c} \left(x - \frac{\lambda m \operatorname{sech}\left(\frac{L}{2\lambda}\right) (c\lambda \cosh\left(\frac{x}{\lambda}\right) - m \sinh\left(\frac{x}{\lambda}\right))}{\Delta} \right)$$

with $\Delta = ac - m^2$. It can be observed that if $m = 0$ the displacement field is independent of a and the classical solution is retrieved.

On Fig. B3 the displacement curve is plotted for different situations. The length and the force are unitary. The material parameters are $c = 100$ N, $a = 5$ N.m² leading to the characteristic length $\lambda \sim 0.22$ m. The three plots, correspond, respectively from the top to the bottom, to the cases in which $m = -20, 0, 20$ N.m. As it should the case $m = 0$ corresponds to the standard situation. The displacement curve is centrosymmetric. Having a non null m parameter breaks this symmetry leading to an heavily distorted displacement field. It can be observed that broken symmetry is somehow contained in the fact that flipping the sign of m amount to inverse the displacement field.

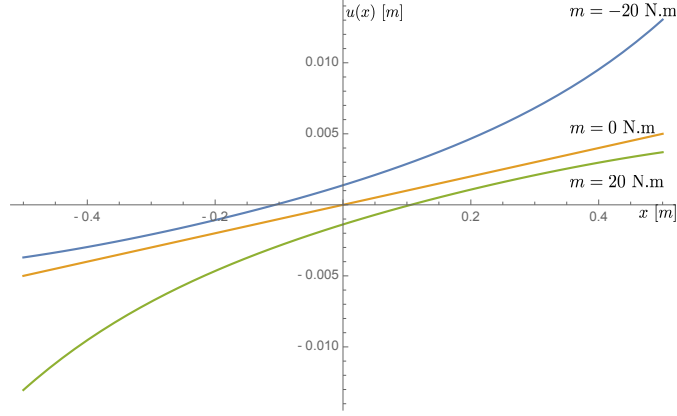


Figure B3: Displacement curve in the 1D continuum. The parameters in common are: $L = 1$ m, $F = 1$ N, $c = 100$ N, $a = 6$ N.m². For m , from top curve to the bottom one: -20 N.m, 0 N.m, 20 N.m. The x -axis (in m) represents the position in the rod, on the y -axis the associated displacement (in m).

The different stress functions inside the continuum have been plotted for the case $m = 20$ N.m on Fig. B4. As can be observed, both the equivalent stress and the hyperstress function are even function of space and hence respect the symmetry of the problem. Hence the symmetry loss seen on kinematic fields is a consequence of the asymmetry of the constitutive law. It can also be noticed that the way σ and τ are distributed in s depends on m and hence on the constitutive law.

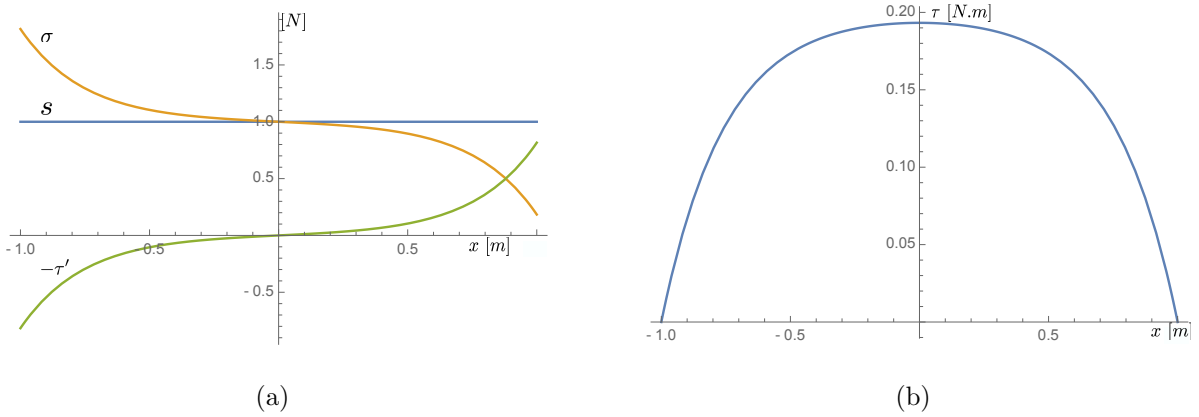


Figure B4: Stress measures in the 1D continuum for the tensile loading. The parameters in common are: $L = 1$ m, $F = 1$ N, $c = 100$ N, 20 N.m, $a = 6$ N.m². Plotted curves represents : Figure (a) from top to bottom, Cauchy stress (N), equivalent stress (N), minus the derivative of the hyperstress (N.m); Figure (b) the hyperstress (N.m). The x -axis (in m) represents the position in the rod.

References

- [1] J.-J. Alibert, F. dell’Isola, and P. Seppecher. Linear elastic trusses leading to con-

- tinua with exotic mechanical interactions. *Continuum Models and Discrete Systems Symposia*, 319:1–13, 2011.
- [2] J.-J. Alibert, P. Seppecher, and F. dell’Isola. Truss modular beams with deformation energy depending on higher displacement gradients. *Mathematics and Mechanics of Solids*, 8(1):51–73, 2003.
- [3] Grégoire Allaire. *Shape optimization by the homogenization method*, volume 146. Springer Science & Business Media, 2012.
- [4] N. Auffray, J. Dirrenberger, and G. Rosi. A complete description of bi-dimensional anisotropic strain-gradient elasticity. *International Journal of Solids and Structures*, 69-70:195–206, 2015.
- [5] G. Besnard, F. Hild, and S. Roux. ”Finite-element” displacement fields analysis from digital images: application to Portevin–Le Chatelier bands. *Experimental Mechanics*, 46(6):789–803, 2006.
- [6] J.P. Boehler, S. Demmerle, and S. Koss. A new direct biaxial testing machine for anisotropic materials. *Exp. Mech.*, 34(1):1–9, 1994.
- [7] M. Bornert, T. Bretheau, and P. Gilormini. *Homogénéisation en mécanique des matériaux, Tome 1 : Matériaux aléatoires élastiques et milieux périodiques*. Hermes Science, 2001.
- [8] C. Boutin. Microstructural effects in elastic composites. *International Journal of Solids and Structures*, 33(7):1023–1051, 1996.
- [9] M. Camar-Eddine and P. Seppecher. Determination of the closure of the set of elasticity functionals. *Archive for rational mechanics and analysis*, 170(3):211–245, 2003.
- [10] J. Cantrell, S. Rohde, D. David Damiani, R. Gurnani, L. DiSandro, J. Anton, A. Young, A. Jerez, D. Steinbach, C. Kroese, and P. Ifju. Experimental characterization of the mechanical properties of 3d printed abs and polycarbonate parts. In *Advancement of Optical Methods in Experimental Mechanics, Volume 3. Conference Proceedings of the Society for Experimental Mechanics Series*. Springer, Cham, 2017.

- [11] E. Cosserat and F. Cosserat. *Théorie des corps déformables*. 1909.
- [12] P. Curie. Sur la symétrie dans les phénomènes physiques, symétrie d'un champ électrique et d'un champ magnétique. *Journal de physique théorique et appliquée*, 3:393–4157, 1894.
- [13] P.G. de Gennes and J. Prost. *The physics of liquid crystals*, volume 83. Oxford university press, 1995.
- [14] F. dell'Isola, G. Sciarra, and S. Vidoli. Generalized Hooke's law for isotropic second gradient materials. *Proceedings of the Royal Society London A*, 465:2177–2196, 2009.
- [15] A. C. Eringen. A unified continuum theory of liquid crystals. *International Journal for Physical and Engineering Sciences*, 50(2):73–84, 1997.
- [16] A.C. Eringen. Mechanics of micromorphic continua. In *Mechanics of generalized continua*, pages 18–35. Springer, 1968.
- [17] I. Gajdos and J. Slota. Influence of printing conditions on structure in FDMx prototypes. *Tehnicki Vjesnik*, 20(2):231–236, 2013.
- [18] J.-S. Gebhardt, A. and Heotter. *Additive Manufacturing. 3D Printing for Prototyping and Manufacturing*. Hanser Gardner Publications, 2016.
- [19] A.E. Green and R.S. Rivlin. Multipolar continuum mechanics. *Archive for Rational Mechanics and Analysis*, 17:113–147, 1964.
- [20] F. Hild and S. Roux. Comparison of local and global approaches to digital image correlation. *Experimental Mechanics*, 52(9):1503–1519, 2012.
- [21] F. Hild, S. Roux, R. Gras, N. Guerrero, M. E. Marante, and J. Florez-Lopez. Displacement measurement technique for beam kinematics. *Optics and Lasers in Engineering*, 47:495–503, 2009.
- [22] H. Leclerc, J. Neggers, F. Mathieu, S. Roux, and F. Hild. Cor-reli 3.0. Agence pour la Protection des Programmes, Paris, 2015. IDDN.FR.001.520008.000.S.P.2015.000.31500.

- [23] R.D. Mindlin. Micro-structure in linear elasticity. *Archive for Rational Mechanics and Analysis*, 16(1), 1964.
- [24] R.D. Mindlin. Second gradient of strain and surface-tension in linear elasticity. *International Journal of Solids and Structures*, 1(4):417–438, 1965.
- [25] R.D. Mindlin and N.N. Eshel. On first strain-gradient theories in linear elasticity. *International Journal of Solids and Structures*, 4(1):109–124, 1968.
- [26] E. Monch and D. Galster. A method for producing a defined uniform biaxial tensile stress field. *Brit. I. Appl. Phys.*, 14:810–812, 1963.
- [27] P. Neff, I. D. Ghiba, A. Madeo, L. Placidi, and G. Rosi. A unifying perspective: the relaxed linear micromorphic continuum. *Wave Motion*, 26(5):639–681, 2014.
- [28] C. Pideri and P. Seppecher. A second gradient material resulting from the homogenization of an heterogeneous linear elastic medium. *Continuum Mechanics and Thermodynamics*, 9(5):241–257, 1997.
- [29] L. Placidi, U. Andreaus, and I. Giorgio. Identification of two-dimensional pantographic structure via a linear d4 orthotropic second gradient elastic model. *Journal of Engineering Mathematics*, pages 1–21, 2016.
- [30] A. Quirk and E. Bevitt. The history, development and application of a uniformly applied load wide plate testing machine. *Nuclear Engineering and Design*, 112:81–91, 1989.
- [31] Y. Rahali, I. Giorgio, J. F. Ganghoffer, and F. dell’Isola. Homogenization à la piola produces second gradient continuum models for linear pantographic lattices. *International Journal of Engineering Science*, pages 148–1725, 2015.
- [32] G. Rosi and N. Auffray. Anisotropic and dispersive wave propagation within strain-gradient framework. *Wave Motion*, 63:120–134, 2016.
- [33] G. Rosi, L. Placidi, and N. Auffray. On the validity range of strain-gradient elasticity: a mixed static-dynamic identification procedure. *Eur. J. Mech. A-Solid*, (-(-):Accepted, 2018.

- [34] S. Roux and F. Hild. Stress intensity factor measurement from digital image correlation: postprocessing and integrated approaches. *International Journal of Fracture*, 140(1-4):141–157, 2006.
- [35] H. Schreier, J.J. Orteu, and M.A. Sutton. *Image correlation for shape, motion and deformation measurements*. Springer US, 2009.
- [36] M. Seidl, J. Safka, J. Bobek, L. Behalek, and J. Habr. Mechanical properties of products made of abs with respect to individuality of fdm production processes. *Modern Machinery Science Journal*, (2):1748–1751, 2017.
- [37] B. Semin, M. L. M. François, and H. Auradou. Analytical shape determination of fiber-like objects with virtual image correlation. *arXiv.org*, (1001.2636):1–17, 2010.
- [38] V.P. Smyshlyaev and K.D. Cherednichenko. On rigorous derivation of strain gradient effects in the overall behaviour of periodic heterogeneous media. *Journal of the Mechanics and Physics of Solids*, 48(6-7):1325–1357, 2000.
- [39] R. A. Toupin. Elastic materials with couple-stresses. *Archive for Rational Mechanics and Analysis*, 11:385–414, 1962.
- [40] H. von Hohenbourg. *Hortus Deliciarum: Manuscript Reconstruction W.Commentary (Studies of the Warburg Institute)*. Warburg Institute, 1979.
- [41] Q.-S. Zheng and J.-P. Boehler. The description, classification, and reality of material and physical symmetries. *Acta Mechanica*, 102(1-4):73–89, 1994.